

A SAMI and MaNGA view on the stellar kinematics of galaxies on the star-forming main sequence

A. Fraser-McKelvie^{1,2,3,4,5,6,7,8,9,10,11,12}★, L. Cortese^{1,2}, J. van de Sande^{2,3}, J. J. Bryant^{2,3,4}, B. Catinella^{1,2},
M. Colless^{1,2,5}, S. M. Croom^{1,2,3}, B. Groves^{1,2}, A. M. Medling^{1,2,6}, N. Scott^{1,2,3}, S. M. Sweet^{1,2,7},
J. Bland-Hawthorn^{1,3}, M. Goodwin⁸, J. Lawrence⁸, N. Lorente⁹, M. S. Owers^{10,11} and S. N. Richards¹²

¹International Centre for Radio Astronomy Research, The University of Western Australia, 35 Stirling Hwy, 6009 Crawley, WA, Australia

²ARC Centre of Excellence for All Sky Astrophysics in 3 Dimensions (ASTRO 3D)

³Sydney Institute for Astronomy (SIfA), School of Physics, The University of Sydney, NSW 2006, Australia

⁴Australian Astronomical Optics, AAO-USydney, School of Physics, University of Sydney, NSW 2006, Australia

⁵Research School of Astronomy and Astrophysics, Australian National University, Canberra ACT 2611, Australia

⁶Ritter Astrophysical Research Center, University of Toledo, Toledo, OH 43606, USA

⁷School of Mathematics and Physics, University of Queensland, Brisbane QLD 4072, Australia

⁸Australian Astronomical Optics – Macquarie, 105 Delhi Rd, North Ryde NSW 2113, Australia

⁹AAO-MQ, Faculty of Science & Engineering, Macquarie University, 105 Delhi Rd, North Ryde NSW 2113, Australia

¹⁰Department of Physics and Astronomy, Macquarie University, NSW 2109, Australia

¹¹Astronomy, Astrophysics and Astrophotonics Research Centre, Macquarie University, Sydney NSW 2109, Australia

¹²SOFIA Science Center, USRA, NASA Ames Research Center, Building N232, M/S 232-12, PO Box 1, Moffett Field, CA 94035-0001, USA

Accepted 2021 February 24. Received 2021 February 23; in original form 2020 December 24

ABSTRACT

Galaxy internal structure growth has long been accused of inhibiting star formation in disc galaxies. We investigate the potential physical connection between the growth of dispersion-supported stellar structures (e.g. classical bulges) and the position of galaxies on the star-forming main sequence at $z \sim 0$. Combining the might of the SAMI and MaNGA galaxy surveys, we measure the λ_{Re} spin parameter for 3289 galaxies over $9.5 < \log M_\star [M_\odot] < 12$. At all stellar masses, galaxies at the locus of the main sequence possess λ_{Re} values indicative of intrinsically flattened discs. However, above $\log M_\star [M_\odot] \sim 10.5$ where the main sequence starts bending, we find tantalizing evidence for an increase in the number of galaxies with dispersion-supported structures, perhaps suggesting a connection between bulges and the bending of the main sequence. Moving above the main sequence, we see no evidence of any change in the typical spin parameter in galaxies once gravitationally interacting systems are excluded from the sample. Similarly, up to 1 dex below the main sequence, λ_{Re} remains roughly constant and only at very high stellar masses ($\log M_\star [M_\odot] > 11$), do we see a rapid decrease in λ_{Re} once galaxies decline in star formation activity. If this trend is confirmed, it would be indicative of different quenching mechanisms acting on high- and low-mass galaxies. The results suggest that whilst a population of galaxies possessing some dispersion-supported structure is already present on the star-forming main sequence, further growth would be required after the galaxy has quenched to match the kinematic properties observed in passive galaxies at $z \sim 0$.

Key words: galaxies: bulges – galaxies: evolution – galaxies: general – galaxies: kinematics and dynamics.

1 INTRODUCTION

Galaxy physical appearance (or morphology) and star formation rate (SFR) are two of the most common properties used to classify galaxies. There is some linkage between the two such that frequently, we see that passive galaxies possess large galactic bulges, whereas star-forming galaxies are more discy in appearance (e.g. Strateva et al. 2001; Driver et al. 2006; Bamford et al. 2009; Bluck et al. 2014; Morselli et al. 2017). Quantifying whether these trends are causal or coincidental is required be-

fore we can fully understand what makes a galaxy stop forming stars.

There is also a very strong correlation between a galaxy's SFR and its stellar mass, M_\star . This correlation means that star-forming galaxies are confined to a narrow sequence (with scatter of order ~ 0.3 dex, see Speagle et al. 2014, and references within) on the $\log(\text{SFR})$ versus $\log(M_\star)$ plane, dubbed the star-forming main sequence (SFMS; Noeske et al. 2007). This fundamental scaling relation covers several dex in stellar mass and describes a (mostly) linear increase in $\log(\text{SFR})$ with $\log(M_\star)$. This relation was in place early (Schreiber et al. 2015; Leslie et al. 2020), and whilst the sequence is tight, the physics of what drives the scatter in the SFMS (especially at high stellar masses) is of great interest.

★ E-mail: a.fraser-mckelvie@uwa.edu.au

Many recent works find that the SFMS relation is not linear across the entire range of stellar masses mapped by extragalactic surveys. Instead, it bends such that high-mass galaxies ($\log M_*(M_\odot) \gtrsim 10.5$ at $z = 0$) possess lower SFRs than projected for their mass based on an extrapolation of the relation for lower-mass galaxies (e.g. Noeske et al. 2007; Bauer et al. 2013; Whitaker et al. 2014, 2015; Schreiber et al. 2015; Tomczak et al. 2016; Leslie et al. 2020). The reason for this decrease in SFR at high stellar masses is unknown, but at low redshifts is thought to be due to a combination of the effects of stellar mass, morphology, and environment (Erfanianfar et al. 2016). Indeed, various works have studied the link between main sequence bending and secular processes such as gas depletion due to environmental effects (e.g. Gavazzi et al. 2015), AGN feedback (e.g. Mancuso et al. 2016; Brennan et al. 2017), halo quenching (e.g. Popesso et al. 2019), or disc rejuvenation (e.g. Mancini et al. 2019).

The growth of a component that increases the stellar mass of a galaxy but not its SFR could also cause the observed decrease in galaxy specific SFR (sSFR) at high stellar masses. For this reason, bulges have also been proposed as a morphological driver of SFMS bending (Wuyts et al. 2011; Abramson et al. 2014; Lang et al. 2014; Whitaker et al. 2015; Erfanianfar et al. 2016). The growth of a dispersion-dominated bulge has also been linked to the cessation of star formation in a galaxy via a morphological quenching pathway (Martig et al. 2009). In this manner, a disc may be stabilized against further fragmentation through the growth of a central mass concentration. However, this paradigm does not explain observations of bulge-dominated galaxies residing in the highly star-forming region of the SFR versus M_* diagram (e.g. Wuyts et al. 2011; Morselli et al. 2017; Popesso et al. 2019).

Bulges can form and grow via multiple pathways, including mergers (e.g. Hopkins et al. 2010), or in a secular manner (e.g. Pfenniger & Norman 1990). Stellar bars are known to play an important role in bulge formation by driving gas into the central regions of galaxies (e.g. Quillen et al. 1995), resulting in starbursts (e.g. Spinoso et al. 2017), and contributing to central mass concentration growth (e.g. Wang et al. 2012). Given bars are disc phenomena, we expect the bulges formed by their influence to be rotation-supported by nature (e.g. Bittner et al. 2020).

But just how can a bulge grow in an actively star-forming galaxy without also quenching the galaxy? ‘Compaction’ describes the growth of a bulge through the movement of galaxies around the main sequence plane through both internal and external processes (e.g. Zolotov et al. 2015; Tacchella et al. 2016). Star-forming galaxies may propagate upwards to be above the SFMS line when an episode of gas infall is triggered (be that by mergers, counter-rotating streams, or violent disc instabilities). During this episode, gas is funnelled to the central regions of a galaxy, where it is used up in a burst of star formation (e.g. Ellison et al. 2018), fuelling the growth of central regions to a saturation point. After this starburst ceases, a galaxy will drop down on to the SFMS (or below) as the gas-depleted galaxy waits to become replenished again. The complex interplay between depletion and replenishment times determines the position of a galaxy on the SFR versus M_* diagram today. In this manner, a galaxy will build up its bulge (and become more compact) through successive compaction events, whilst remaining on the SFMS. Importantly, the process of compaction sets no constraints on bulge kinematics.

One of the results of compaction should be a population of bulge-dominated galaxies that lie above the SFMS. (Morselli et al. 2017; Popesso et al. 2019). Some studies, however, do not find this, (e.g. Cook et al. 2020), and rather attribute the bulge-dominated

starbursting galaxies to poor bulge-disc decompositions, often complicated by mergers and interactions. These same works that suggest bulge growth as the cause of SFMS bending also report that this process is not sufficient to produce the amount of bending seen at high stellar masses (Popesso et al. 2019). Indeed, main sequence bending has also been seen in populations of visually classified pure disc galaxies (Guo et al. 2015). These studies suggest that a decrease in the SF activity of the disc is also required, and various environmental mechanisms including virial shock heating (e.g. Birnboim & Dekel 2003; Kereš et al. 2005) or gravitational infall heating (e.g. Dekel & Birnboim 2008; Khochfar & Ostriker 2008) have been proposed to provide this additional star formation quenching.

Whatever the cause of the SFMS bending, we do know that the scatter in the SFMS likely reflects a real diversity in star formation histories (Abramson et al. 2014; Matthee & Schaye 2019). Extending on this idea, we might also expect a variety of stellar kinematics, indicative of a variety of galaxy formation pathways. Previous work has shown a link between Hubble type and the spin parameter λ_{Re} (Cortese et al. 2016; Falcón-Barroso et al. 2019; Wang et al. 2020), V/σ (van de Sande et al. 2018), and specific angular momentum (Cortese et al. 2016), such that later-type spiral galaxies are more rotationally supported than earlier-type spirals and S0s. Wang et al. (2020) extended on this idea by examining the link between galaxy visual morphology and position on the SFMS. A picture emerged in which galaxies lying on the SFMS were predominantly spirals with small bulges, whilst below the SFMS, galaxy kinematics depended on stellar mass (though it should be noted that our own Milky Way violates this picture with a small bulge, but low SFR for its stellar mass e.g. Licquia & Newman 2015). Wang et al. (2020) reported a strong mass dependence below the SFMS such that low-mass galaxies were ‘fast rotator’ early-type galaxies, whilst high-mass ($M_* > 2 \times 10^{11} M_\odot$) galaxies were ‘slow rotator’ spheroids.

A dichotomy at $z = 0$ between star-forming, disc-dominated galaxies and passive, bulge-dominated galaxies is apparent. What is unclear however, is the order of these processes. Can a bulge form in a star-forming galaxy (and does it have a role in the quenching of star formation), or is bulge build-up the realm of passive galaxies?

In this paper, we investigate kinematic trends across the SFMS with IFS data, comparing galaxy spin parameters both on and off the SFMS. For this sort of analysis, we will benefit from the number statistics that the two largest IFS surveys to date can provide, and so we combine data from both the Sydney-AAO Multi-object Integral field spectrograph (SAMi; Croom et al. 2012) galaxy survey and the Mapping Nearby Objects at APO (MaNGA; Bundy et al. 2015) galaxy survey. Given that the target selection of these two surveys differ, we are able to probe more of the galaxy parameter space, and compare whether or not trends seen in one data set persist between the two. To enable the best comparison possible, we measure kinematic properties between the two surveys using a homogeneous set of structural parameters, SFR measurements, and stellar mass indicators.

This paper is organized as follows: in Section 2, we describe the SAMi and MaNGA IFS surveys, along with the homogeneous structural parameters used to calculate kinematic measurements. We also describe the IFS sample, kinematic measurement and corrections, along with the definition of the main sequence line used. In Section 3, we present the results, and in Section 4, we discuss the implications of our findings. Throughout this paper we employ a Λ CDM cosmology, with $\Omega_m = 0.3$, $\Omega_\Lambda = 0.7$, $H_0 = 70 \text{ km s}^{-1} \text{ Mpc}^{-1}$ and a Chabrier (2003) IMF.

2 DATA AND METHODS

2.1 The SAMI galaxy survey

The SAMI galaxy survey is an IFS survey on the Anglo-Australian Telescope (AAO) that observed 3068 galaxies from 2013 to 2018 (Croom et al. 2012). SAMI uses 13 fused fibre hexabundles (Bland-Hawthorn et al. 2011; Bryant et al. 2014) with a high (75 per cent) fill factor. Each bundle contains 61 fibres of 1.6" diameter resulting in each integral field unit (IFU) having a diameter of 15". The IFUs, as well as 26 sky fibres, are plugged into pre-drilled plates using magnetic connectors. SAMI fibres are fed to the double-beam AAOmega spectrograph (Sharp et al. 2015), which allows a range of different resolutions and wavelength ranges. The SAMI Galaxy survey employs the 570V grating at 3750–5750 Å giving a resolution of $R = 1810$ ($\sigma = 70.4 \text{ km s}^{-1}$) at 4800 Å, and the 1000 R grating from 6300–7400 Å giving a resolution of $R = 4260$ ($\sigma = 29.6 \text{ km s}^{-1}$) at 6850 Å (Scott et al. 2018). 83 per cent of galaxies in the SAMI target catalogue have coverage out to $1R_e$ (Bryant et al. 2015).

The SAMI survey is comprised of a sample drawn from the GAMA equatorial regions (Bryant et al. 2015), and an additional sample of eight clusters (Owers et al. 2017). SAMI Data Release 3 (DR3; Croom et al. 2021) contains observations of 3068 galaxies and is the final data release of the SAMI survey. SAMI DR3 includes observations spanning $0.04 < z < 0.128$ and $7.42 < \log M_\star [M_\odot] < 11.89$ (corresponding to an r -band magnitude range of $18.4 < m_r < 12.1$), with environments ranging from underdense field regions to extremely overdense clusters.

SAMI DR3 galaxy cubes are provided for use, along with an array of maps data products. All data products have spaxel size of $0.5'' \text{ spaxel}^{-1}$, and the average seeing FWHM is $\sim 2''$. Here, we employ the two-moment Gaussian line of sight velocity distribution (LOSVD) stellar kinematic maps (van de Sande et al. 2017b), including rotational velocity, and velocity dispersion (σ) maps. We use the adaptively binned maps, in which spaxels are binned to a signal-to-noise (S/N) of 10 using the Voronoi binning code of Cappellari & Copin (2003). The S/N is calculated from the flux and variance spectra of each spaxel as the median across the entire blue wavelength range (Scott et al. 2018), and spaxels with $S/N > 10$ are not binned.

2.2 The MaNGA galaxy survey

The MaNGA Galaxy Survey is an IFS survey that observed $> 10\,000$ galaxies from 2014 to 2020 (Bundy et al. 2015; Drory et al. 2015). It is an SDSS-IV project (Blanton et al. 2017), employing the 2.5 m telescope at Apache Point Observatory (Gunn et al. 2006) and BOSS spectrographs (Smee et al. 2013), which have continuous wavelength coverage from 3600–10 300 Å at $R \sim 2700$ ($\sigma \sim 70 \text{ km s}^{-1}$). MaNGA's target galaxies were chosen to include a wide range of galaxy masses and colours, over the redshift range $0.01 < z < 0.15$. The Primary+ sample (Yan et al. 2016a; Wake et al. 2017) contains galaxies with spatial coverage out to $\sim 1.5R_e$ for ~ 66 per cent of the total sample, and the remainder (dubbed the Secondary sample) are observed out to $\sim 2.5R_e$, generally at higher redshifts than the Primary+ sample. SDSS-IV data release 15 (DR15; Aguado et al. 2019) contains 4621 unique galaxies, selected in the range $7.9 < \log M_\star [M_\odot] < 12.1$, (corresponding to $18.1 < m_r < 11.6$), and a range of field environments, observed and reduced by the MaNGA Data Reduction Pipeline (Law et al. 2015). Derived properties are produced by the MaNGA Data Analysis Pipeline (DAP; Westfall et al. 2019), provided as a single data cube per galaxy

(Yan et al. 2016b). MaNGA's spaxel size matches that of SAMI, at $0.5'' \text{ spaxel}^{-1}$, and the average seeing conditions throughout the survey were such that the r -band PSF FWHM is $\sim 2.5''$.

We employ the two-moment LOSVD stellar velocity and dispersion maps using the Voronoi binning scheme to ensure each bin reaches a target S/N of 10. We also apply the velocity dispersion correction provided to account for MaNGA instrumental dispersion (see Westfall et al. 2019).

2.3 Star formation rates and stellar masses

In this analysis, we wish to compare trends in the spin parameter λ_{Re} with current star formation activity in galaxies. Given there may be observational biases that are unaccounted for between the two surveys, we report trends in SAMI and MaNGA data separately. However, to determine a robust star-forming main sequence line, we wish to be able to place the two surveys on a homogeneous $\text{SFR}-M_\star$ plane.

For this reason, we match both SAMI DR3 and MaNGA DR15 to the GALEX-Sloan-WISE legacy catalogue 2 (GSWLC-2; Salim et al. 2016; Salim, Boquien & Lee 2018) using a sky match with maximum separation of $2''$. GSWLC-2 provides UV–optical–mid-infrared (IR) SED-derived stellar masses and SFRs for 659 229 galaxies within the SDSS footprint and $z < 0.3$, with photometry provided by GALEX, SDSS, and the Wide-Field Survey Explorer (WISE). We utilize the GSWLC-X2 catalogue, which uses the deepest GALEX photometry available (selected from the shallow ‘all-sky’, medium-deep, and deep catalogues) for a source in the SED fit. SED fitting was performed using the Code Investigating GALaxy Emission (CIGALE; Noll et al. 2009; Boquien et al. 2019), which constrains SED fits with IR luminosity, which they term SED+LIR fitting.

3901 MaNGA galaxies have matches to the GSWLC-2, and 1832 SAMI galaxies. Unfortunately many of the galaxies lost belong to the SAMI cluster sample, though we note that four clusters have GSWLC-2 coverage.

2.4 Structural parameters

To enable a comparison between SAMI and MaNGA kinematic quantities, we require the structural parameters used to define the apertures to be identical. Indeed, a small change in aperture size can result in an appreciable difference in λ_{Re} values for a given galaxy. For this reason, we match both surveys to the NASA-Sloan Atlas (NSA; Blanton et al. 2011), and use the elliptical Petrosian values for effective radius (R_e), axial ratio (b/a), which we use to define the ellipticity, ϵ , as $\epsilon = 1 - b/a$, photometric galaxy position angle (ϕ), and the Sérsic index (n) from a single Sérsic fit. As MaNGA's targeting catalogue was the NSA, all galaxies have these values available. 1831 SAMI galaxies with GSWLC-2 data also have counterparts in the NSA.

2.5 Defining a star-forming main sequence

We define the SFMS line for the SAMI and MaNGA galaxies used in this work by fitting a curve to the points at which the number density is highest in the SFR versus M_\star diagram in bins of stellar mass over the mass range $9 < \log M_\star [M_\odot] < 11.7$. For each bin of stellar mass, we simply determine the peak of a histogram of SFRs. In order to increase number statistics, whilst still fitting to the overall SAMI and MaNGA galaxy distribution, we fit this curve to the GSWLC-2 sample over the redshift range of the SAMI and MaNGA samples. We also weight the GSWLC-2 galaxy sample

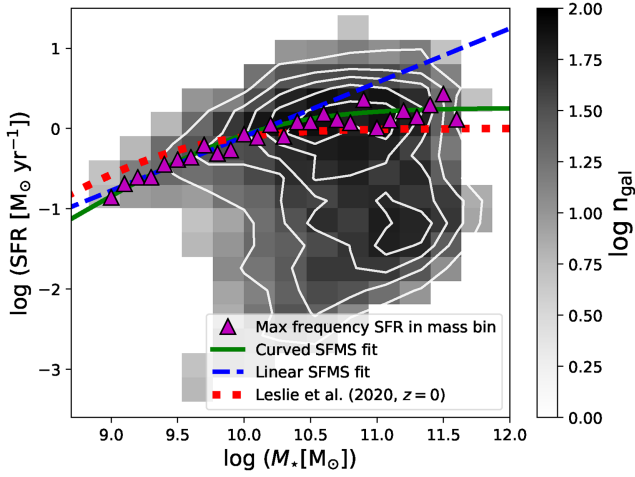


Figure 1. A 2D histogram of the number of galaxies (n_{gal}) in bins of stellar mass and star formation rate for the combined SAMI and MaNGA sample. Contours of the overall distribution of the sample are overlaid in white. The SFMS line is fit to GSWLC-2 galaxies that match the overall redshift distribution of SAMI and MaNGA, and magenta markers denote the peak of the SFR distribution for that mass bin. The SFMS line of equation (3) is shown in green and the linear SFMS line fit of equation (4) is shown in blue. For comparison, the SFMS fit of Leslie et al. (2020) extrapolated to $z = 0$ is shown in red.

such that the overall redshift distribution of the SAMI and MaNGA samples is also matched. This increases the number of galaxies used in the fit from ~ 5700 in the SAMI and MaNGA sample to $\sim 403\,000$. In this manner, the main sequence line naturally bends at high stellar masses, as shown in Fig. 1. We fit the functional form of the main sequence curve definition introduced in Leslie et al. (2020) (which is based on that of Lee et al. 2015):

$$\log(\langle SFR [M_{\odot} \text{ yr}^{-1}] \rangle) = S_0 - a_1 t - \log_{10} \left(1 + \frac{10^{M'_t}}{10^M} \right), \quad (1)$$

$$M'_t = M_0 - a_2 t, \quad (2)$$

where M is $\langle \log(M_*/M_{\odot}) \rangle$, M'_t is the turnover mass, and t is the age of the Universe in Gyr. For star-forming galaxies, Leslie et al. (2020) find $S_0 = 2.97^{+0.08}_{-0.09}$, $M_0 = 11.06^{+0.15}_{-0.16}$, $a_1 = 0.22^{+0.01}_{-0.01}$, and $a_2 = 0.12^{+0.03}_{-0.02}$. We use these values, along with $t = 13.5$ Gyr, and fit a curve to the star-forming galaxies (defined arbitrarily as those with $\log(SFR) > 0.704 \times \log(M_*) - 8.21$) in the GSWLC-2 using SCIPY'S OPTIMIZE.CURVEFIT package. The best-fitting main sequence line for the SAMI and MaNGA galaxies is:

$$\log(SFR [M_{\odot} \text{ yr}^{-1}]) = 0.256 - \log_{10} \left(1 + \frac{10^{10.064}}{10^M} \right), \quad (3)$$

where M is as defined above.

We note that equation (3) deviates at high stellar masses towards slightly higher SFRs compared to the Leslie et al. (2020) curve, as shown in Fig. 1; similar SFMS behaviour is also reported in Thorne et al. (2020). The Leslie et al. (2020) SFMS relation is derived from 3GHz radio continuum imaging of the COSMOS field, and is extrapolated below $z \sim 0.3$. The high-mass objects observed at low redshift in this work are not present in the Leslie et al. (2020) sample, and we speculate this is the reason behind the discrepancies at the high-mass end.

As a comparison, we also fit a linear main sequence line to investigate any biases introduced by the assumption that the main

sequence bends at high stellar masses. We use only low-mass galaxies in the linear main sequence fit, (where there is no obvious deviation from a straight line, see Fig. 1) within the mass range $9.0 < \log M_* [M_{\odot}] < 10.0$. The best-fitting straight line to the GSWLC-2 galaxies scaled to match the redshift distribution of the combined SAMI and MaNGA sample is:

$$\log(SFR [M_{\odot} \text{ yr}^{-1}]) = (0.674 \times M) - 6.836, \quad (4)$$

where M is as defined above. The results of this paper using a linear SFMS line are presented in Appendix A.

We define the quantity Δ MS as the difference in SFR from the prediction of the SFMS curve of equation (3) for a galaxy of the same mass.

2.6 λ_{Re} measurement

Following Emsellem et al. (2007) and Emsellem et al. (2011), we define the spin parameter approximation, λ_{Re} , as the flux-weighted ratio of ordered to disordered motion within a galaxy:

$$\lambda_R = \frac{\langle R|V| \rangle}{\langle R\sqrt{V^2 + \sigma^2} \rangle} = \frac{\sum_{i=0}^{N_{\text{sp}}} F_i R_i |V_i|}{\sum_{i=0}^{N_{\text{sp}}} F_i R_i \sqrt{V_i^2 + \sigma_i^2}}, \quad (5)$$

where F is the flux, V the stellar rotational velocity, and σ the stellar velocity dispersion of the i th spaxel. In the same manner as Cortese et al. (2016) and van de Sande et al. (2017b), we define R as the semi-major axis of an ellipse on which spaxel i lies. We chose to use the intrinsic radius rather than the circular projected radius as it follows the galaxy light profile more accurately. We note that whilst this is the same technique used for SAMI galaxies by van de Sande et al. (2017b), the values of ϵ , R_e , and ϕ used to define the ellipse within which λ_{Re} is calculated are different. The reason for this difference is that we wish to compare SAMI and MaNGA measurements in as close a manner as possible, and hence used the same catalogue (the NSA) for structural measurements of galaxies for both surveys. This discrepancy results in a small scatter of order ~ 0.05 in λ_{Re} measurements (though importantly, no offset) between the λ_{Re} values from van de Sande et al. (2017b) and those reported in this work.

At this point, some cuts were also applied to the SAMI and MaNGA data to ensure only galaxies with reliable kinematics were included in the λ_{Re} catalogue. In both samples, we removed galaxies with R_e less than the HWHM PSF of the observation. For MaNGA, we also removed galaxies for which more than 20 per cent of spaxels within an ellipse of semi-major axis $1R_e$ were masked. The masking could be the result of flags introduced in the data reduction process (as the DAP velocity and σ masks were applied to the maps prior to analysis), or we also masked all spaxels where the corrected $\sigma < 50 \text{ km s}^{-1}$, as Westfall et al. (2019) suggests that this is the lower limit for which dispersion measurements can be trusted when $S/N > 10$.

SAMI kinematic quality cuts are described in section 3.2.6 of van de Sande et al. (2017b), and involve a relative σ cut such that bad spaxels are defined as those with $\sigma_{\text{error}} > \sigma \times 0.1 + 25 \text{ km s}^{-1}$. We keep the same quality cuts as van de Sande et al. (2017b), and reject any galaxy with > 25 per cent bad spaxels from the following analysis. In addition, we removed any galaxies for which R_e is greater than the aperture size (~ 16 per cent of the sample), to avoid the need for aperture corrections, and those that were flagged as having unreliable kinematics in the SAMI DR3 kinematics catalogue.

In Fig. 2, we show histograms of the combined SAMI and MaNGA parent sample with GSWLC-2 SFRs (grey histograms), and the

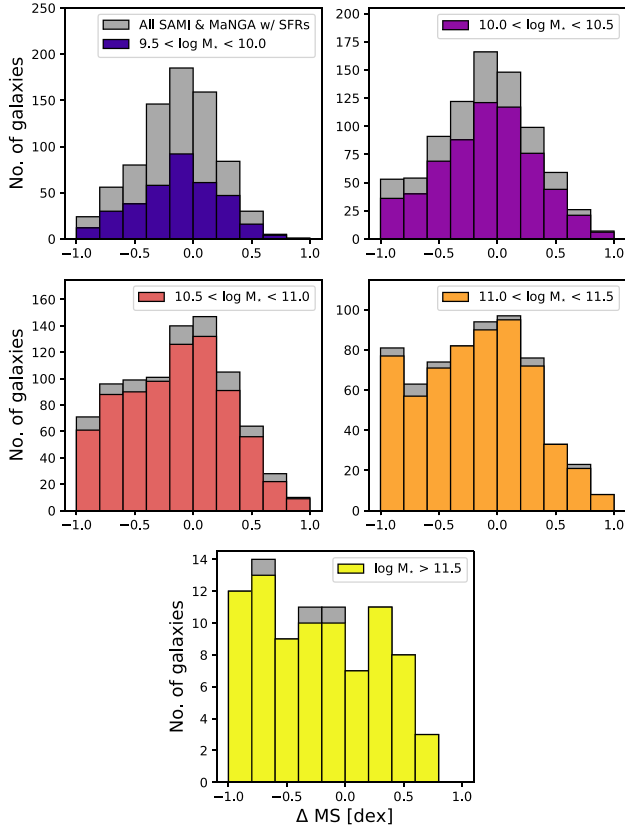


Figure 2. The effects of the kinematic sample selection cuts on the parent sample of SAMI and MaNGA galaxies with GSWLC-2 SFRs. Each panel is a histogram of the distribution of the distance of a galaxy to the main sequence line (ΔMS) in five mass bins, with the parent sample in grey, and the final sample of galaxies used for kinematic analysis after quality cuts were made in colour. The majority of galaxies rejected from the kinematic analysis are low-mass, and this is mostly due to low continuum S/N.

final kinematic sample used in this analysis after all cuts are made (coloured histograms). Each panel of Fig. 2 represents a mass bin used in this work. Unsurprisingly, the greatest number of galaxies are lost from the low stellar mass bins, mostly due to poor continuum S/N within the galaxy. Our final samples are representative and highly complete (84 per cent) for $\log M_* [M_\odot] > 10$, though the completeness drops significantly (to 48 per cent) for $\log M_* [M_\odot] < 10$. Whilst we still cover the entire range of SFRs of interest for our analysis, we recommend caution in extrapolating our findings to the entire low mass population. In summary, 897 SAMI galaxies and 2392 MaNGA galaxies have reliable λ_{Re} measurements.

2.7 Inclination and seeing corrections

Measurement of the λ_{Re} parameter is influenced by both the FWHM of the PSF of the observation and the galaxy inclination angle (e.g. Cappellari 2016; Graham et al. 2018), hence we attempt to account for both of these effects. Given the difference in average seeing conditions between the SAMI (FWHM $\sim 2''$) and MaNGA (FWHM $\sim 2.5''$) surveys, it is essential to apply a seeing correction so that we may facilitate as close a comparison in kinematic properties as possible. There are several recent examples of seeing corrections for IFS data in the literature (e.g. Graham et al. 2018; Chung, Park & Park 2020; Harborne et al. 2020). We decide to apply the seeing

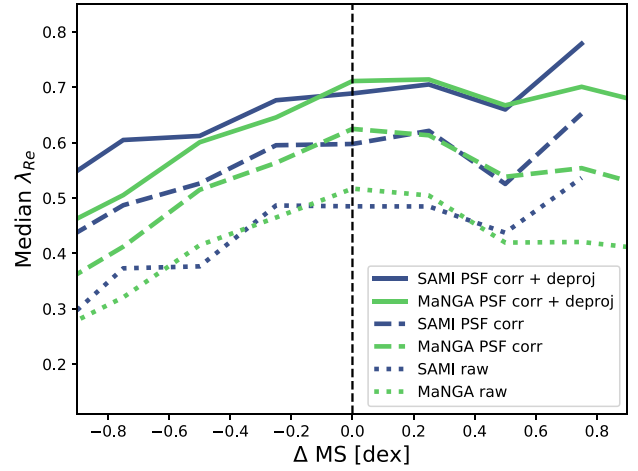


Figure 3. The effect of the PSF and inclination corrections on the spin parameter λ_{Re} . Navy lines indicate SAMI median values, and green MaNGA. Dotted lines denote the raw median λ_{Re} values, dashed lines are after the PSF-correction of Harborne et al. (2020), and solid lines are median λ_{Re} values in bins of ΔMS after PSF-correction and deprojection.

correction of Harborne et al. (2020),¹ due in part to its ease of application to different IFS survey data sets. Briefly, the corrections of Harborne et al. (2020) take the Sérsic index of the galaxy and FWHM of the IFS observation and provide a value for λ_{Re} that is corrected for seeing. Given the MaNGA PSF is on average $\sim 0.5''$ greater than that of SAMI, the PSF corrections affect the MaNGA data more. Fig. 3 shows the increase in median λ_{Re} after both PSF correction (an increase of ~ 0.1 , in line with Graham et al. 2018) and deprojection corrections are applied as a function of distance from the main sequence (ΔMS) for SAMI (navy blue lines) and MaNGA (green lines) galaxies. Although the corrections change the absolute value of the median λ_{Re} , the overall shape of the curves are preserved, meaning that the relative ordering of the spin parameter values will not change greatly when kinematic corrections are applied.

Fig. 4 shows that for the combined SAMI and MaNGA sample, there is a dependence on galaxy axial ratio (b/a) with ΔMS such that galaxies above the main sequence are rounder than those on the main sequence (assuming that b/a indicates inclination and not intrinsic shape). As pointed out by Wang et al. (2020), without an inclination correction the raw rotational stellar velocity and σ values propagate to artificially low λ_{Re} values above the main sequence, making these galaxies appear more dispersion-dominated than they actually are.

Many deprojection corrections exist in the literature ranging from a simple $1/\sqrt{\epsilon}$ (e.g. Cortese et al. 2016), to more complicated functions (e.g. Falcón-Barroso et al. 2019). We chose the correction of Emsellem et al. (2011), as implemented by del Moral-Castro et al. (2020):

$$\lambda_{R}^{deproj} = \frac{\lambda_R}{\sqrt{C^2 - \lambda_R^2(C^2 - 1)}}; \quad (6)$$

$$C = \frac{\sin i}{\sqrt{1 - \beta \cos^2 i}}; \quad (7)$$

$$\cos i = \sqrt{\frac{(b/a)^2 - q_0^2}{1 - q_0^2}} \quad (8)$$

¹http://github.com/katcharborne/kinematic_corrections

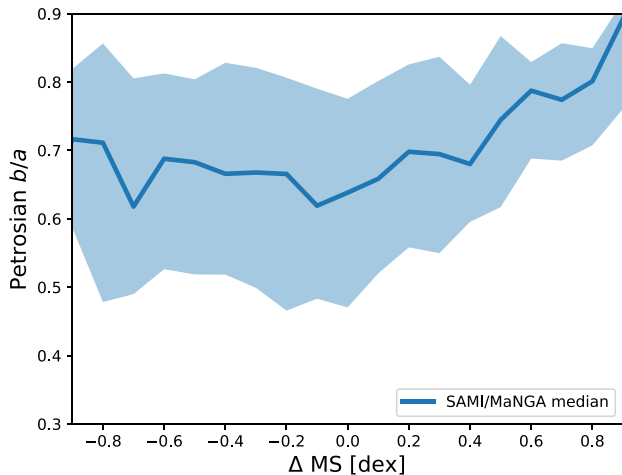


Figure 4. Petrosian axial ratio, b/a , of the combined SAMI/MaNGA kinematic sample for bins of ΔMS . The shaded region denotes the 25th and 75th percentiles of the distribution. Galaxies above the main sequence are on average more round than those on or below.

where b/a is the axial ratio of the galaxy, and q_0 is the intrinsic axial ratio of an edge-on galaxy. As we are interested primarily in galaxies on or near the star-forming main sequence, we choose $q_0 = 0.2$, as used in Cortese et al. (2016) for galaxies with a clear disc component. The anisotropy parameter, β , varies slightly with Hubble type, but we use $\beta = 0.3$, which is appropriate for disc galaxies (derived from table B.1 of Kalinova et al. 2017).

We note that previous studies have found variation in both the q_0 and β parameters with galaxy morphology (e.g. Cappellari et al. 2007; Chemin 2018). We tested the difference between SAMI $\lambda_{Re,deproj}$ values using fixed q_0 and β and those where q_0 and β varied with galaxy morphology obtained from the catalogue of Cortese et al. (2016). We found very little difference between the two methods, with the maximum $\Delta\lambda_{Re,deproj}$ of ~ 0.03 . Importantly, there are no trends in median $\lambda_{Re,deproj}$ with ΔMS . In addition, van de Sande et al. (in preparation), show that there is very little offset ($\Delta\lambda_{Re} < 0.05 - 0.1$) in deprojected λ_{Re} measures between using the simplistic assumptions presented above and a more detailed approach as described by Cappellari et al. (2007).

Given the similarity between the fixed and morphology-based deprojection values coupled with the fact that we do not have a homogeneous morphology catalogue for both the SAMI and MaNGA samples, we stick with the assumption of $q_0 = 0.2$ and $\beta = 0.3$.

Fig. 3 shows that whilst the overall shape of the λ_{Re} distribution as a function of ΔMS remains similar, on average, MaNGA λ_{Re} values are slightly higher ($\Delta\lambda_{Re, PSF\ corr + deproj} \sim 0.05$) than SAMI at $\Delta MS = 0$. There could be multiple reasons for this discrepancy, one of which being simply a difference in sample selection. That said, the locus of the main sequence should be well sampled by both surveys. A difference in the median S/N may also be the result of MaNGA sampling more of the disc regions of galaxies that are missed by SAMI. Whilst poorly sampled galaxies are removed from the kinematic samples and we always measure λ out to $1R_e$, if MaNGA is sampling slightly more spaxels per galaxy on average than SAMI, this may result in a slightly higher median λ_{Re} measurement. Finally, another possible reason for the λ_{Re} discrepancy may be the way in which stellar velocity and σ were derived between surveys. Whilst SAMI broadens their spectra to that of the templates used for a continuum fit, MaNGA fits at the native

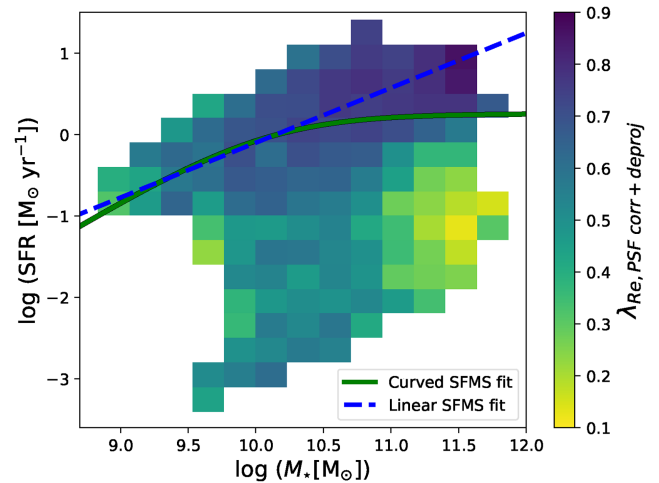


Figure 5. A 2D histogram of median λ_{Re} for bins of stellar mass and star formation rate for the combined SAMI and MaNGA sample. The SFMS line of equation (3) is shown in green, and for comparison, the linear main sequence line fit to low-mass galaxies of equation (4) is shown in blue.

resolution, then applies a dispersion correction after fitting to account for instrumental dispersion effects. Both of these methods produce velocity and σ measurements that convey the astrophysical Doppler broadening, though it is possible that the differing techniques result in slight differences between the resultant derived velocity and σ measurements.

There is currently no galaxy that is observed in both SAMI DR3 and MaNGA DR15 releases, but we note that if this changes in the future [indeed, Law et al. (2020) found 74 galaxies in common between the internal MaNGA Product Launch 10 (MPL-10) and SAMI DR2], a detailed analysis into any discrepancies between velocity and σ measures will be extremely informative. Additionally, performing the analysis of this work on simulated SAMI and MaNGA kinematic data will give insight into the origin of any small differences seen in the kinematics between the two surveys.

3 RESULTS

3.1 λ_{Re} on the SFMS

After performing the various sample cuts described in Section 2, the SAMI sample spans $0.01 < z < 0.11$, $9.5 < \log M_* [M_\odot] < 11.8$, $17.8 < m_r < 12.1$, and the MaNGA sample $0.01 < z < 0.15$, $9.5 < \log M_* [M_\odot] < 12.1$, $17.5 < m_r < 11.6$.

In Fig. 5, we present a 2D histogram of the SFR versus M_* plane for both the SAMI and MaNGA samples with bins coloured by the average PSF-corrected and deprojected λ_{Re} values. The main sequence line defined in equation (3) is shown in green. In line with Croom et al. (in preparation), overall trends are readily visible: the passive, high-mass galaxies are chiefly dispersion-dominated systems, and the rotation-dominated systems populate the main sequence line regions of the plot. Interestingly, the range of λ_{Re} values is greatest at the highest stellar masses: high-mass galaxies are both the most rotation-dominated and the most dispersion-dominated galaxies in the local Universe.

We plot the median λ_{Re} as a function of ΔMS for the SAMI kinematic sample in Fig. 6, and for the MaNGA kinematic sample in Fig. 7, where only bins that contain five or more galaxies are displayed. As a comparison, we plot the same parameters in

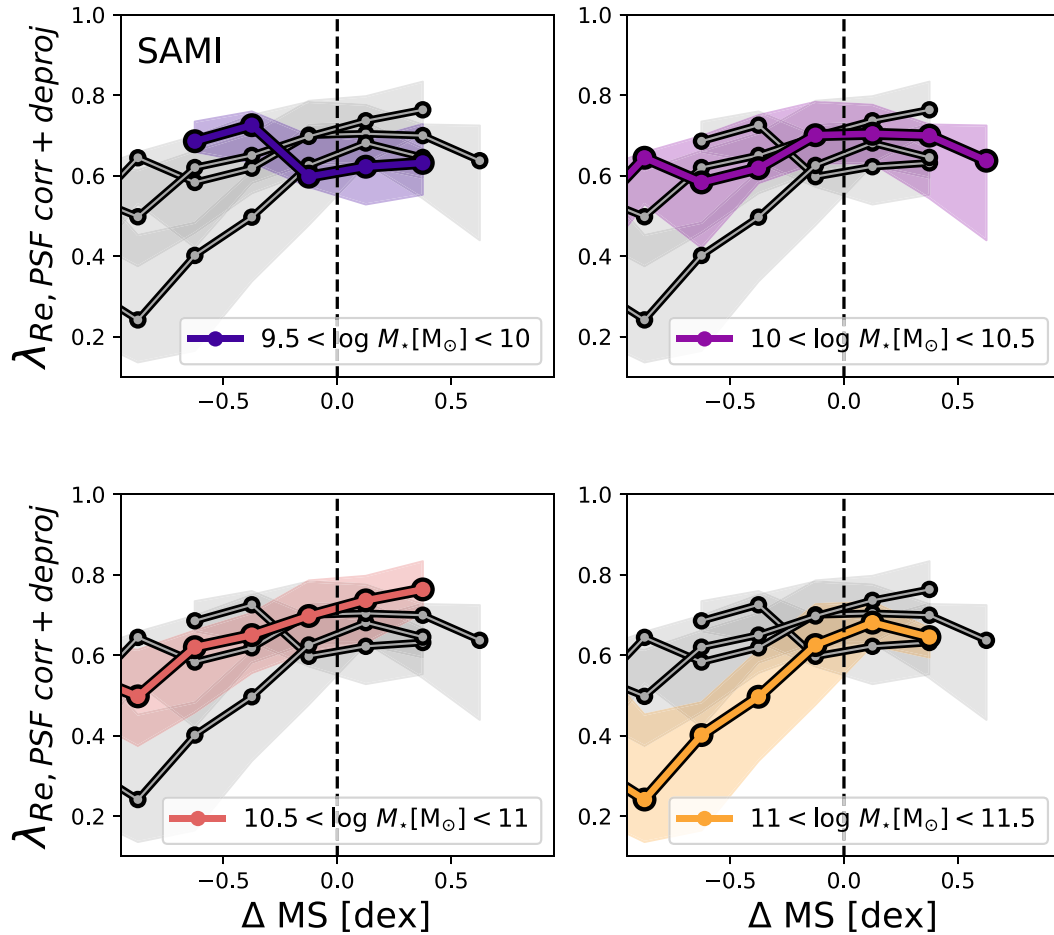


Figure 6. Median λ_{Re} for SAMI galaxies as a function of distance from the SFMS line of equation (3) (ΔMS) in bins of stellar mass. Each panel highlights a different mass bin, with all other mass bins shown in grey for comparison. Shaded regions denote the 25th and 75th percentiles for each mass bin. The vertical dashed line denotes the locus of the main sequence. In general, the SFMS is populated by discy galaxies, with little change in λ_{Re} within ± 1 dex of the SFMS for all but the most massive galaxies.

Figs A1 and A2, but calculating ΔMS using the linear fit to low-mass galaxies from equation (4). In both Figures, each panel highlights a mass bin, with all others shown for comparison in grey. Shaded regions denote the 25th and 75th percentiles. Due to increased sample statistics at the high-mass end, there is an extra high-mass bin for the MaNGA sample that is not present for the SAMI data. For both the SAMI and MaNGA results in Figs 6 and 7, we see that at the locus of the main sequence ($\Delta MS = 0$), the median λ_{Re} value is high. Galaxies on the main sequence are rotationally supported systems, in line with previous photometric (e.g. Wuyts et al. 2011; Morselli et al. 2017) and spectroscopic (Oh et al. 2020; Wang et al. 2020) structural studies. Both SAMI and MaNGA suggest an increase of λ_{Re} with stellar mass for main sequence galaxies. Specifically, the median λ_{Re} increases from ~ 0.65 for $9.5 < \log M_* [M_\odot] < 10$ to ~ 0.75 for $10.5 < \log M_* [M_\odot] < 11$ at $\Delta MS = 0$ for MaNGA galaxies. Overall, we see a hint of mass dependence for λ_{Re} such that the slope of the median λ_{Re} as a function of ΔMS becomes steeper at higher stellar masses.

Above the main sequence, the SAMI sample does not show any significant change in the median value of the stellar spin parameter.

However, this sample does not probe beyond $\Delta MS \sim 0.4$ dex. Conversely, MaNGA allows us to reach $\Delta MS \sim 0.8$ dex where, at least for stellar masses $9.5 < \log M_* [M_\odot] < 11$, we find marginal evidence for a decrease in λ_{Re} in very strongly star-forming galaxies. Whilst intriguing, this decrease is only marginally significant, and given the tendency of tidal interactions triggering starbursts, potentially more indicative of disturbances in the stellar velocity field than gradual thickening of the disc or build-up of a dispersion-dominated stellar component.

Indeed, if we remove the 27 galaxies that clearly show signs of gravitational interaction in their SDSS optical images from the highest two bins of ΔMS for the MaNGA sample, the decrease in stellar spin at high ΔMS reduces somewhat. In Fig. 7, solid lines depict the full MaNGA kinematic sample, and dotted lines are the MaNGA sample with obvious interactions removed from the highest two ΔMS bins in the right panel. All disturbed SAMI galaxies were already removed from the sample when the quality control cuts were applied. Fig. 7 confirms that especially for stellar masses $10 < \log M_* [M_\odot] < 11$, the median λ_{Re} value flattens out slightly above the main sequence. We note that we removed only the most obviously interacting systems whose SDSS images showed extreme

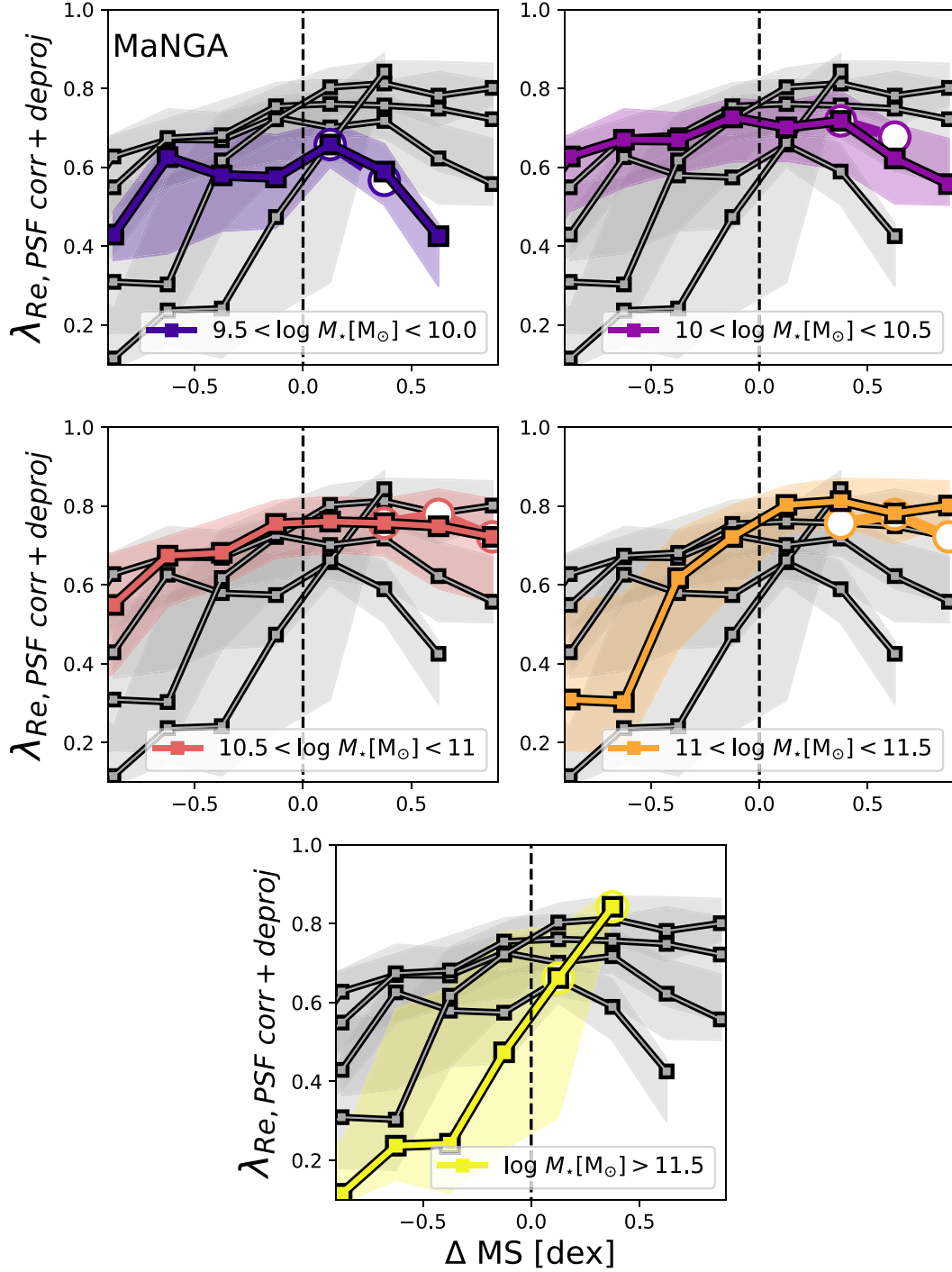


Figure 7. Median λ_{Re} for MaNGA galaxies as a function of distance from the SFMS line of equation (3) (ΔMS) in bins of stellar mass. Each panel highlights a different mass bin, with all other mass bins shown in grey for comparison. Shaded regions denote the 25th and 75th percentiles for each mass bin. Solid lines depict the full MaNGA kinematic sample, and dotted lines with white circles are the MaNGA sample with obvious interactions removed from the highest two ΔMS bins. The extra high-mass bin for MaNGA galaxies is due to the greater number of high-mass galaxies in this sample.

warping from tidal interaction. There are likely many interacting systems of varying degrees of tidal disruption still remaining within the MaNGA kinematic sample.

Below the main sequence, the picture emerging is slightly different. For galaxies with stellar masses $9.5 < \log M_* [M_\odot] < 10.5$,

stellar spin seems to remain roughly constant up to ~ 1 dex below the locus of the main sequence. At higher stellar masses, both SAMI and MaNGA seem to suggest a steepening of the $\Delta MS - \lambda_{Re}$ relation so that with increasing mass, low stellar spin galaxies become more frequent closer to the locus of the main sequence.

4 DISCUSSION

4.1 A discy main sequence

We first discuss trends seen for star-forming galaxies located on the main sequence. The most striking observation from Figs 6 and 7 is that apart from the highest stellar mass bin of $\log M_* [\text{M}_\odot] > 11.5$, all galaxies on the main sequence ($\Delta \text{MS} = \pm 0.25$ dex) possess λ_{Re} values indicative of discy galaxies ($0.6 < \lambda_{Re, \text{PSF corr} + \text{deproj}} < 0.8$). As there is a strong link between the λ_{Re} spin parameter and the intrinsic shape of a galaxy (e.g. Foster et al. 2017), we can therefore infer that galaxies on the main sequence are intrinsically flattened and axisymmetric discs. Apart from perhaps the highest mass bins, galaxies on the main sequence are as rotationally supported and intrinsically flattened as they will get; the main sequence is populated by the disciest galaxies.

For the MaNGA galaxies in Fig. 7, we see a small mass dependence at $\Delta \text{MS} = 0$ such that apart from the highest mass bin (within which dispersion-dominated structures may be beginning to dominate) there is the trend that on average, higher-mass galaxies have greater values of λ_{Re} than low mass. Catinella, Giovanelli & Haynes (2006) show that the rotation curves of high-mass galaxies reach their peaks at shorter disc scale-lengths than low-mass dwarfs, making it more likely that the flat region of their rotation curves are contained within $1R_e$. Given the λ_{Re} metric effectively normalizes galaxy spin by stellar mass (thanks to the σ in the denominator of equation 5), on average, the peak velocity of a galaxy's rotation curve should be contained within the $1R_e$ aperture of high-mass galaxies more frequently than for their low-mass counterparts. Hence, the resultant λ_{Re} value will be greater. This observation may explain the mass dependence seen at the locus of the main sequence.

4.2 Classical bulge growth above the main sequence?

Recent photometric studies of galaxies above the main sequence report that the bulge-to-total ratio (B/T) increases such that starbursting galaxies are more bulge-dominated than their neighbours on the main sequence (Morselli et al. 2017; Popesso et al. 2019). These studies find that starbursting galaxies possess highly star-forming central regions, which from concentration measures they infer are resultant from the growth of classical bulges. We are able to test this theory from a kinematic standpoint.

Whilst we do observe a slight reduction in median λ_{Re} above the main sequence, this reduces when we remove the 27 galaxies from the MaNGA sample that are obviously interacting according to their SDSS colour images. These interacting galaxies will likely be highly dispersion-supported due to the random motions of stars induced by merger activity. Of course interactions act to decrease the rotational support of a galaxy whilst often inducing starburst activity, however these motions are not necessarily indicative of classical bulge growth. Galaxy interactions may therefore be artificially lowering the median spin parameter value above the main sequence.

We re-examine trends in the $\lambda_{Re} - \Delta \text{MS}$ relation of Fig. 7 above the main sequence once interacting galaxies are removed. For all but the highest and lowest stellar mass bins, the median λ_{Re} curves flatten somewhat such that they are similar both on and above the main sequence, and these values are for that of dynamically cold, discy systems. Our results show that there is very little decrease in λ_{Re} for the majority of non-interacting systems above the main sequence, and from this we imply that we do not see evidence of classical bulge growth in this regime.

The finding that dispersion-dominated bulges are not growing above the main sequence for the majority of the galaxy population does not preclude a compaction scenario. Rather, it is constrained such that the episode of gas infall must occur in a manner so as not to disrupt the rotationally supported nature of the inner regions of a galaxy. We speculate that the gas infall event that triggers a central burst of star formation must be ordered. An investigation into the ordered and random motions of gas in the central regions of galaxies above the main sequence should reveal just how turbulent the gas infall episode is.

We note that the SAMI and MaNGA samples do not probe the extreme starbursting galaxy population. Our results are statistically significant up to $+0.8$ dex above the SFMS, whilst photometric studies such as Morselli et al. (2017) report B/T trends up to $+1$ dex above the SFMS. Given these trends, we should still expect to see some evidence of dispersion-dominated structure growth in the highest two ΔMS bins of our kinematic results. We do see some evidence for a decrease in spin parameter, but we attribute this to a small number of interacting galaxies, rather than large-scale classical bulge growth.

One such explanation for the discrepancy between the kinematic results presented here and photometric results from the literature is from the photometric decomposition technique. Cook et al. (2020) showed that the structural decomposition technique used can affect B/T measurements across a large mass range. From a careful structural decomposition of a relatively small sample of galaxies, Cook et al. (2020) found a monotonic decrease in B/T above the main sequence for all but the lowest-mass galaxies in their sample. They attributed the observed differences to spurious structural measurements stemming from the limited model validation available for large (SDSS-sized) catalogues of bulge-disc decompositions. Indeed, mergers and interacting galaxies are traditionally very difficult to fit with simple bulge+disc models (e.g. Mezcuza et al. 2014). Our work agrees qualitatively with that of Cook et al. (2020): we do not find evidence of a population of starburst galaxies with systematically higher B/T in the local Universe.

A caveat to this work is the spatial resolution of the IFS observations; it is possible that these galaxies on and above the main sequence do not have bulges large enough to be seen in the stellar kinematics. The PSF of SAMI and MaNGA are $\sim 2''$ and $\sim 2.5''$ respectively, which both correspond to 2.0 kpc at the median redshifts of the kinematic samples used in this work of $z = 0.05$ and $z = 0.04$. Dispersion-dominated bulges significantly smaller than 2 kpc may be washed out through beam-smearing effects. Whilst this should not be a problem for higher-mass galaxies, classical bulges located in lower-mass galaxies can indeed possess sub-kpc bulge effective radii (Gadotti 2009).

These results can be linked to the structural growth and morphological transformation within galaxies in the context of star formation. Given that we see no growth of dispersion-supported structure on the SFMS, and yet passive galaxies host such structures (especially at high stellar masses), we may say something about the link between galaxy quenching and morphological transformation via dispersion-dominated bulge growth. Our results are consistent with two scenarios: the first where initial quenching must take place *before* morphological transformation, and the second where if these two processes are concurrent, then the timescales differ such that morphological transformation occurs more slowly than quenching (or at least the galaxy moving off the main sequence; e.g. Cortese et al. 2019). We are not in a position to say which scenario is occurring, but Croom et al. (in preparation) take a

different approach in attempting to explain the formation of S0 galaxies via a combination of photometric concentration measures and kinematic dispersion parametrization. In this manner, they find that S0 formation can be explained via a simple disc fading model taking into account progenitor bias. These results may provide clues about bulge growth in the wider galaxy population.

4.3 Classical bulge growth below the main sequence?

Figs 6 and 7 show a steepening of the $\lambda_{Re} - \Delta$ MS relation with increasing stellar mass below the SFMS. The reason behind this steepening is unclear: whilst it seems to be revealing an increase in dispersion-supported structure dominance, it could also be the result of an upward scatter in SFRs due to the inherent unreliability of SFR indicators at low sSFRs.

Separating star-forming and passive galaxies becomes increasingly difficult at higher stellar masses. As can be seen from Fig. 1, the clear bi-modality of star-forming and passive populations seen between $10.5 < \log M_* [M_\odot] < 11.0$ diminishes at higher stellar masses. Coupled with a bending of the SFMS towards lower SFRs, it becomes difficult to determine where the main sequence is sampling star-forming galaxies, and where the green valley begins. Indeed, works that define an SFMS through Gaussian mixture modelling have increasing difficulty fitting two Gaussians (one for the star-forming population and one for the passive population) at high stellar masses (e.g. Popesso et al. 2019). Whether this blending of populations in the SFR plane is physical or the result of unreliable SFR indicators at low sSFR is unknown. If the latter, then we might expect some passive galaxies to artificially inhabit the lower portion of main sequence regions. This effect would be strongest at high stellar masses for a curved main sequence, as it is in these regions that the main sequence line deviates to lower sSFRs. The observed steepening of the $\lambda_{Re} - \Delta$ MS relation may be explained by a portion of passive galaxies (with dominant dispersion-supported structure) contaminating the λ_{Re} measures below the SFMS. Indeed, the steepening of the $\lambda_{Re} - \Delta$ MS relation with mass practically disappears if we use a linear fit to the main sequence.

If the observed steepening of the $\lambda_{Re} - \Delta$ MS slope is real, then this would suggest that the mechanisms acting on high- and low-mass galaxies as they become more passive are different: one produces passive galaxies with similar disc structure as when they were on the main sequence, whilst the other must dramatically alter the kinematics of a galaxy. The obvious mechanism that will destroy or thicken a disc is mergers. Interestingly, the vast majority of slow rotator galaxies possess high stellar masses (e.g. Emsellem et al. 2007; van de Sande et al. 2017a, 2020; Graham et al. 2018; Wang et al. 2020). It is tempting to speculate that the reason for the λ_{Re} steepening in high-mass galaxies only may be that either the mergers required to create them only occur in high-mass galaxies, or perhaps the processes of mass build up as the result of mergers differ with stellar mass (e.g. Robotham et al. 2014). Both of these processes must begin whilst the galaxy is still on the SFMS.

One subject that this work does not touch on is the effect of environment on the degree of dispersion support within galaxies as a function of their sSFR. Hence, an exciting avenue for follow-up work on this topic is through exploring trends with centrals versus satellite galaxies.

4.4 The cause of main sequence bending

Many works propose the growth of bulges as the driver of main-sequence bending (e.g. Abramson et al. 2014; Popesso et al. 2019).

Already we see a hint in Fig. 7 that the highest-mass galaxies (the regime in which we expect the greatest deviation from a linear main sequence) are more dispersion-dominated. We are in a unique position to test this theory from a kinematic standpoint by examining whether we see any differences in the Δ MS values of high- and low- λ_{Re} galaxies.

We split the combined SAMI and MaNGA sample between $-0.8 < \Delta \text{ MS} < 0.8$ into low ($\lambda_{Re} < 0.6$) and high ($\lambda_{Re} > 0.6$) λ_{Re} sub-samples. We note here that the low λ_{Re} sample does not consist solely of dispersion-dominated systems, rather they are simply *more* dispersion-supported than the high λ_{Re} systems. There are also trends present with stellar mass such that higher-mass galaxies are more likely to possess greater dispersion support. This means that there will be a greater number of high-mass galaxies in the low- λ_{Re} sample, and lower-mass galaxies in the high- λ_{Re} sample. In Fig. 8, we plot the distribution of Δ MS for low λ_{Re} (red line) and high λ_{Re} (blue line) galaxies as a function of distance from the curved SFMS line defined in equation (3). As a comparison, we plot the distribution of the overall sample in grey. The locus of the SFMS is shown by a black dashed line.

At low stellar masses, we see that the Δ MS distribution is very similar for all values of λ_{Re} , though the low- λ_{Re} systems begin to deviate above $\log M_* [M_\odot] = 10$, and at high masses are preferentially located below the SFMS line. Similarly, above $\log M_* [M_\odot] = 11$, the high- λ_{Re} systems begin to deviate above the overall Δ MS distribution. At high-mass, systems with greater dispersion dominance preferentially populate regions below the SFMS line (however it is defined), whilst rotation-dominated systems sit above. We interpret these trends as evidence that the ‘bending’ region of the SFMS is populated by galaxies of greater dispersion support – high-mass galaxies with greater dispersion support are more likely to possess lower SFRs than their more rotationally dominated counterparts.

Our findings suggest that dispersion-dominated bulges are already present in massive galaxies on the main sequence. This is not surprising, given that the existence of visually classified early-type (i.e. possessing a prominent bulge component) star-forming spirals has been known since the establishment of the Hubble morphological sequence. That said, the growth of a dispersion dominated bulge is not the only possible cause of a decrease in λ_{Re} : disc thickening will also decrease λ_{Re} . When our results are coupled with photometric work highlighting the redistribution of stars towards central regions below the main sequence however (e.g. Morselli et al. 2017; Popesso et al. 2019), they are sufficient to expect that at least some of the λ_{Re} decrease is due to bulge growth.

It is very tempting to push the interpretation of our results further and wonder if they provide direct evidence of a physical link between lower SFRs and the growth of dispersion-dominated structure in high-mass galaxies. The morphological quenching argument of Martig et al. (2009) suffices in explaining the lower SFRs seen in high-mass galaxies with greater dispersion support. These galaxies possess lower SFRs because their bulges are large enough that they have begun to stabilize galaxy discs against further star formation. A similar explanation was put forward by both Whitaker et al. (2015) and Erfanianfar et al. (2016) to explain the morphology dependence on the scatter in the main sequence, and a flatter main sequence for galaxies with high Sérsic index respectively. It is also possible that the lower sSFR is due to the growth of a non-star-forming component that adds to the stellar mass of a galaxy without increasing its SFR. In this case, the growth of a bulge and the cessation of star formation do not need to be linked. Whatever the cause, we are left with an intriguing hint of the role of morphology in regulating a galaxy’s star formation. We can certainly conclude that the bending of the SFMS

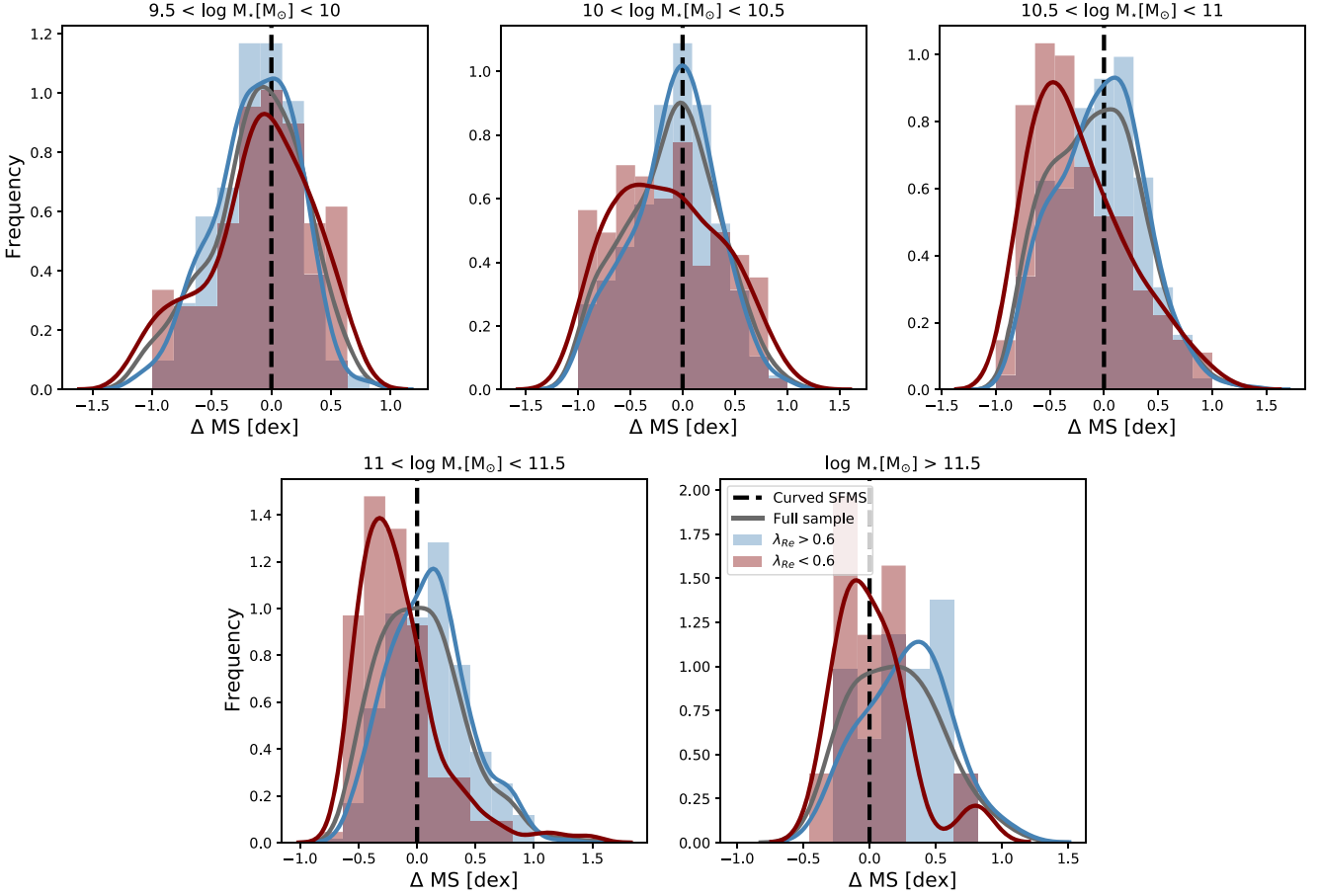


Figure 8. Histograms and their associated kernel density estimate (KDE) plots of the combined SAMI and MaNGA kinematic sample (grey), galaxies with $\lambda_{Re} > 0.6$ (blue), and $\lambda_{Re} < 0.6$ (red) in bins of stellar mass for $-1 < \Delta MS < 1$. $\Delta MS = 0$ is shown in black. At low stellar masses, there is no deviation away from the main sequence. At higher stellar masses, low λ_{Re} galaxies deviate towards lower sSFRs, whilst high λ_{Re} galaxies move above the main sequence line. We interpret these trends as evidence that more dispersion-dominated galaxies populate the ‘bending’ region of the SFMS.

at high stellar masses is coincident with a population of galaxies that possess classical bulges.

5 SUMMARY AND CONCLUSIONS

We search for evidence of kinematic transformation in galaxies on the SFMS by examining the link between galaxy SFR and stellar kinematics from IFS observations. Combining the might of the SAMI and MaNGA IFS galaxy surveys, we calculate the spin parameter, λ_{Re} , in a homogenized manner for 3289 galaxies. Our main results are:

(i) **Galaxies on the SFMS possess λ_{Re} values indicative of intrinsically flattened discs.** There is a small mass trend such that higher-mass galaxies appear to have higher λ_{Re} values than lower-mass galaxies, which we expect is due to the peak of low-mass galaxy velocity fields being more likely to occur outside the $1R_e$ aperture used in this work.

For the highest stellar mass bin ($\log M_* [M_\odot] > 11.5$), we see a population of galaxies on the SFMS that possess a small dispersion-dominated bulge component (and possibly some contribution from a thickened disc).

(ii) **No decrease in λ_{Re} above the SFMS.** Once interacting galaxies are removed, λ_{Re} measurements up to $+0.8$ dex above the SFMS are consistent with those on the SFMS for the majority of galaxies (though we see marginal evidence that this may not

hold true for the lowest-mass galaxies of $9.5 < \log M_* [M_\odot] < 10$), from which we conclude that there is no growth of dispersion-dominated galaxy components whilst a galaxy is in a starburst phase. If compaction is occurring in highly star-forming galaxies, it cannot be contributing to classical bulge growth.

(iii) **A decrease in λ_{Re} below the SFMS for high-mass ($\log M_* [M_\odot] > 11$) galaxies.** One possibility for the decrease in median λ_{Re} below the SFMS may be that the SFR indicator is unreliable at low sSFRs, scattering some green valley galaxies to higher SFRs than they should be. If the trend is real however, then quenching mechanisms must differ between high- and low-mass galaxies: low-mass galaxies are quenching without structure growth, whilst some mechanism is acting to both quench a galaxy and dramatically adjust the stellar kinematics at $\log M_* [M_\odot] > 11$. The likely culprit is gravitational interactions.

(iv) **Evidence for a tantalizing phenomenological connection between the bending of the SFMS and an increase in galaxy dispersion support.** Lower λ_{Re} galaxies are preferentially located on or below the SFMS line for $\log M_* [M_\odot] > 10.5$. More rotationally supported systems ($\lambda_{Re} > 0.6$) better follow a linear SFMS line. The bending of the SFMS is primarily due to the fact that lower λ_{Re} galaxies start dominating the galaxy budget of the SFMS at high stellar masses, which we speculate is evidence for the growth of classical bulges.

Our results indicate that bulge growth is occurring in high-mass galaxies on and just below the SFMS to some degree. In addition, we see evidence that the growth of a dispersion-dominated bulge is linked to the bending of the SFMS at high stellar masses. Whilst extremely promising, we note that further investigation is still required to precisely identify the link between the SFMS bending and an increase in dynamical pressure support. Despite our observations, bulge growth is minor for the majority of galaxies on the SFMS. Given that most extremely massive passive galaxies are slow rotators, we find that extra bulge growth is still required once a galaxy has quenched to produce the red and dead S0s observed in the local Universe today.

ACKNOWLEDGEMENTS

The SAMI Galaxy Survey is based on observations made at the Anglo-Australian Telescope. The Sydney-AAO Multi-object Integral field spectrograph (SAMI) was developed jointly by the University of Sydney and the Australian Astronomical Observatory. The SAMI input catalogue is based on data taken from the Sloan Digital Sky Survey, the GAMA Survey, and the VST ATLAS Survey. The SAMI Galaxy Survey is supported by the Australian Research Council Centre of Excellence for All Sky Astrophysics in 3 Dimensions (ASTRO 3D), through project number CE170100013, the Australian Research Council Centre of Excellence for All-sky Astrophysics (CAASTRO), through project number CE110001020, and other participating institutions. The SAMI Galaxy Survey website is <http://sami-survey.org/>. LC is the recipient of an Australian Research Council Future Fellowship (FT180100066) funded by the Australian Government. JvdS acknowledges support of an Australian Research Council Discovery Early Career Research Award (project number DE200100461) funded by the Australian Government. NS acknowledges support of an Australian Research Council Discovery Early Career Research Award (project number DE190100375) funded by the Australian Government and a University of Sydney Postdoctoral Research Fellowship. Parts of this research were conducted by the Australian Research Council Centre of Excellence for All Sky Astrophysics in 3 Dimensions (ASTRO 3D), through project number CE170100013. JJB acknowledges support of an Australian Research Council Future Fellowship (FT180100231). JBH is supported by an ARC Laureate Fellowship and an ARC Federation Fellowship that funded the SAMI prototype. AMM acknowledges support from the National Science Foundation under Grant No. 2009416. MSO acknowledges the funding support from the Australian Research Council through a Future Fellowship (FT140100255).

DATA AVAILABILITY

The SAMI data presented in this paper are available from Astronomical Optics' Data Central service at: <https://datacentral.org.au/>. The MaNGA data are available at: <https://www.sdss.org/dr15/manga/ma-nga-data/data-access/>.

REFERENCES

- Abramson L. E., Kelson D. D., Dressler A., Poggianti B., Gladders M. D., Oemler A., Jr, Vulcani B., 2014, *ApJ*, 785, L36
- Aguado D. S. et al., 2019, *ApJS*, 240, 23
- Bamford S. P. et al., 2009, *MNRAS*, 393, 1324
- Bauer A. E. et al., 2013, *MNRAS*, 434, 209
- Birnboim Y., Dekel A., 2003, *MNRAS*, 345, 349
- Bittner A. et al., 2020, *A&A*, 643, A65
- Bland-Hawthorn J. et al., 2011, *Optics Express*, 19, 2649
- Blanton M. R., Kazin E., Muna D., Weaver B. A., Price-Whelan A., 2011, *AJ*, 142, 31
- Blanton M. R. et al., 2017, *AJ*, 154, 28
- Bluck A. F. L., Mendel J. T., Ellison S. L., Moreno J., Simard L., Patton D. R., Starkenburg E., 2014, *MNRAS*, 441, 599
- Boquien M., Burgarella D., Roehlly Y., Buat V., Ciesla L., Corre D., Inoue A. K., Salas H., 2019, *A&A*, 622, A103
- Brennan R. et al., 2017, *MNRAS*, 465, 619
- Bryant J. J., Bland-Hawthorn J., Fogarty L. M. R., Lawrence J. S., Croom S. M., 2014, *MNRAS*, 438, 869
- Bryant J. J. et al., 2015, *MNRAS*, 447, 2857
- Bundy K. et al., 2015, *ApJ*, 798, 7
- Cappellari M., 2016, *ARA&A*, 54, 597
- Cappellari M., Copin Y., 2003, *MNRAS*, 342, 345
- Cappellari M. et al., 2007, *MNRAS*, 379, 418
- Catinella B., Giovanelli R., Haynes M. P., 2006, *ApJ*, 640, 751
- Chabrier G., 2003, *PASP*, 115, 763
- Chemin L., 2018, *A&A*, 618, A121
- Chung H., Park C., Park Y.-S., 2020, preprint ([arXiv:astro-ph/2008.04313](https://arxiv.org/abs/2008.04313))
- Cook R. H. W., Cortese L., Catinella B., Robotham A., 2020, *MNRAS*, 493, 5596
- Cortese L. et al., 2016, *MNRAS*, 463, 170
- Cortese L. et al., 2019, *MNRAS*, 485, 2656
- Croom S. M. et al., 2012, *MNRAS*, 421, 872
- Croom S. M. et al., 2021, preprint ([arXiv:2101.12224](https://arxiv.org/abs/2101.12224))
- Dekel A., Birnboim Y., 2008, *MNRAS*, 383, 119
- del Moral-Castro I. et al., 2020, *A&A*, 639, L9
- Driver S. P. et al., 2006, *MNRAS*, 368, 414
- Drory N. et al., 2015, *AJ*, 149, 77
- Ellison S. L., Sánchez S. F., Ibarra-Medel H., Antonio B., Mendel J. T., Barrera-Ballesteros J., 2018, *MNRAS*, 474, 2039
- Emsellem E. et al., 2007, *MNRAS*, 379, 401
- Emsellem E. et al., 2011, *MNRAS*, 414, 888
- Erfanianfar G. et al., 2016, *MNRAS*, 455, 2839
- Falcón-Barroso J. et al., 2019, *A&A*, 632, A59
- Foster C. et al., 2017, *MNRAS*, 472, 966
- Gadotti D. A., 2009, *MNRAS*, 393, 1531
- Gavazzi G. et al., 2015, *A&A*, 580, A116
- Graham M. T. et al., 2018, *MNRAS*, 477, 4711
- Gunn J. E. et al., 2006, *AJ*, 131, 2332
- Guo K., Zheng X. Z., Wang T., Fu H., 2015, *ApJ*, 808, L49
- Harborne K. E., van de Sande J., Cortese L., Power C., Robotham A. S. G., Lagos C. D. P., Croom S., 2020, *MNRAS*, 497, 2018
- Hopkins P. F. et al., 2010, *ApJ*, 715, 202
- Kalinova V. et al., 2017, *MNRAS*, 469, 2539
- Kereš D., Katz N., Weinberg D. H., Davé R., 2005, *MNRAS*, 363, 2
- Khochfar S., Ostriker J. P., 2008, *ApJ*, 680, 54
- Lang P. et al., 2014, *ApJ*, 788, 11
- Law D. R. et al., 2015, *AJ*, 150, 19
- Law D. R. et al., 2020, preprint ([arXiv:2011.04675](https://arxiv.org/abs/2011.04675))
- Lee N. et al., 2015, *ApJ*, 801, 80
- Leslie S. K. et al., 2020, *ApJ*, 899, 58
- Licquia T. C., Newman J. A., 2015, *ApJ*, 806, 96
- Mancini C. et al., 2019, *MNRAS*, 489, 1265
- Mancuso C., Lapi A., Shi J., Cai Z.-Y., Gonzalez-Nuevo J., Béthermin M., Danese L., 2016, *ApJ*, 833, 152
- Martig M., Bournaud F., Teyssier R., Dekel A., 2009, *ApJ*, 707, 250
- Matthee J., Schaye J., 2019, *MNRAS*, 484, 915
- Mezcua M., Lobanov A. P., Mediavilla E., Karouzos M., 2014, *ApJ*, 784, 16
- Morselli L., Popesso P., Erfanianfar G., Concas A., 2017, *A&A*, 597, A97
- Noeske K. G. et al., 2007, *ApJ*, 660, L43
- Noll S., Burgarella D., Giovannoli E., Buat V., Marcellac D., Muñoz-Mateos J. C., 2009, *A&A*, 507, 1793
- Oh S. et al., 2020, *MNRAS*, 495, 4638
- Owers M. S. et al., 2017, *MNRAS*, 468, 1824
- Pfenniger D., Norman C., 1990, *ApJ*, 363, 391

Popesso P. et al., 2019, *MNRAS*, 483, 3213
 Quillen A. C., Frogel J. A., Kenney J. D. P., Pogge R. W., Depoy D. L., 1995, *ApJ*, 441, 549
 Robotham A. S. G. et al., 2014, *MNRAS*, 444, 3986
 Salim S. et al., 2016, *ApJS*, 227, 2
 Salim S., Boquien M., Lee J. C., 2018, *ApJ*, 859, 11
 Schreiber C. et al., 2015, *A&A*, 575, A74
 Scott N. et al., 2018, *MNRAS*, 481, 2299
 Sharp R. et al., 2015, *MNRAS*, 446, 1551
 Smee S. A. et al., 2013, *AJ*, 146, 32
 Speagle J. S., Steinhardt C. L., Capak P. L., Silverman J. D., 2014, *ApJS*, 214, 15
 Spinoso D., Bonoli S., Dotti M., Mayer L., Madau P., Bellovary J., 2017, *MNRAS*, 465, 3729
 Strateva I. et al., 2001, *AJ*, 122, 1861
 Tacchella S., Dekel A., Carollo C. M., Ceverino D., DeGraf C., Lapiner S., Mandelker N., Primack Joel R., 2016, *MNRAS*, 457, 2790
 Thorne J. E. et al., 2020, preprint (arXiv:2011.13605)
 Tomczak A. R. et al., 2016, *ApJ*, 817, 118
 van de Sande J. et al., 2017a, *MNRAS*, 472, 1272
 van de Sande J. et al., 2017b, *ApJ*, 835, 104
 van de Sande J. et al., 2018, *Nat. Astron.*, 2, 483
 van de Sande J. et al., 2020, preprint (arXiv:2011.08199)
 Wake D. A. et al., 2017, *AJ*, 154, 86
 Wang J. et al., 2012, *MNRAS*, 423, 3486
 Wang B., Cappellari M., Peng Y., Graham M., 2020, *MNRAS*, 495, 1958

Westfall K. B. et al., 2019, *AJ*, 158, 231
 Whitaker K. E. et al., 2014, *ApJ*, 795, 104
 Whitaker K. E. et al., 2015, *ApJ*, 811, L12
 Wuyts S. et al., 2011, *ApJ*, 742, 96
 Yan R. et al., 2016a, *AJ*, 151, 8
 Yan R. et al., 2016b, *AJ*, 152, 197
 Zolotov A. et al., 2015, *MNRAS*, 450, 2327

APPENDIX A: LINEAR MAIN SEQUENCE

We present median λ_{Re} in bins of stellar mass as a function of Δ MS using the *linear* definition of the SFMS line from equation (4). Fig. A1 shows the SAMI results, and Fig. A2 are the MaNGA results.

It is worth noting that the increase of λ_{Re} with stellar mass at the locus of the main sequence described in Section 3 remains even if Δ MS is measured from the linear fit to the SFMS. The only difference is the change in behaviour at the highest stellar mass bins, simply because we no longer have galaxies at these stellar masses on the SFMS.

Interestingly, the trend of a steepening of the Δ MS – λ_{Re} relation below the main sequence almost entirely disappears (or is at least pushed towards higher distances from the main sequence) when a linear fit to the main sequence is used.

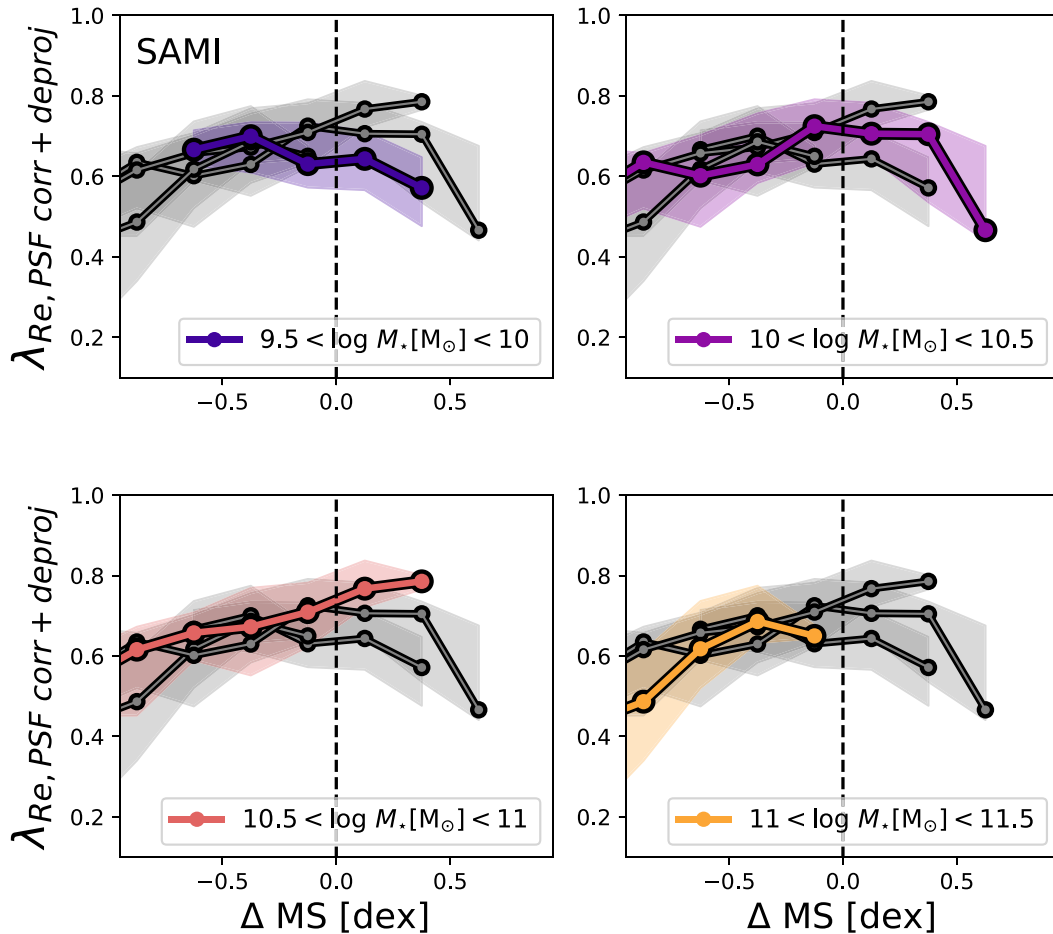


Figure A1. Same as Fig. 6, but using the linear SFMS line equation (4) to calculate Δ MS. Given there are fewer galaxies above the linear SFMS line, we are not able to probe as far above the main sequence as with the curved line.

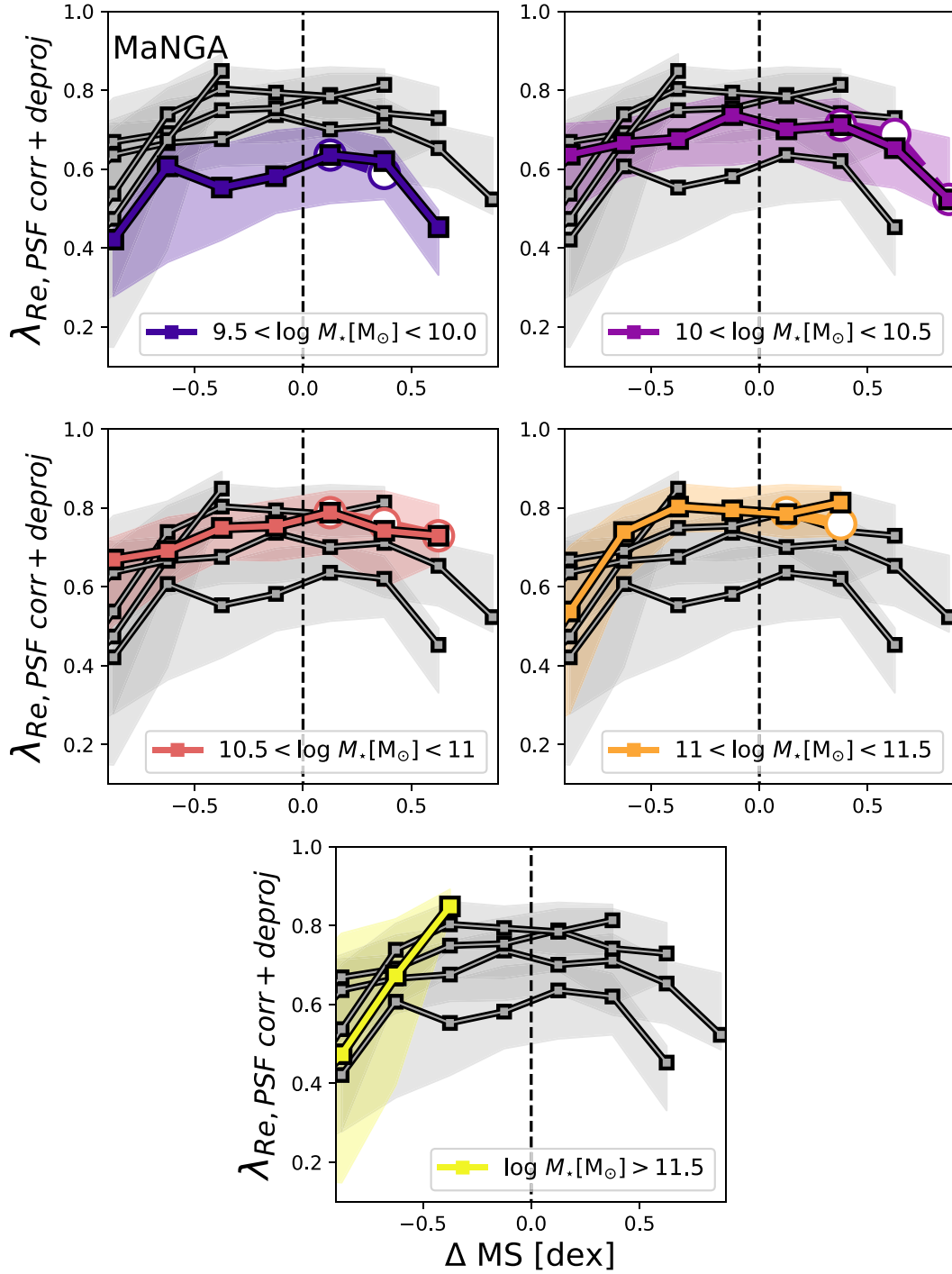


Figure A2. Same as Fig. 7, but using the linear main sequence line of equation (4) to calculate ΔMS . Given there are fewer galaxies above the linear SFMS line, we are not able to probe as far above the main sequence as with the curved line.

This paper has been typeset from a \LaTeX file prepared by the author.